Photochemical & Photobiological Sciences
https://doi.org/10.1007/s43630-022-00233-z

ORIGINAL PAPERS

Accumulation of mono-reduced [Ir(piq)$_2$(LL)] photosensitizers relevant for solar fuels production

Martin Wodon[1] · Simon De Kreijger[1] · Renato N. Sampaio[2] · Benjamin Elias[1] · Ludovic Troian-Gautier[1]

Received: 27 January 2022 / Accepted: 13 April 2022
© The Author(s), under exclusive licence to European Photochemistry Association, European Society for Photobiology 2022

Abstract
A series of nine [Ir(piq)$_2$(LL)]$^+$.PF$_6^-$ photosensitizers, where piqH = 1-phenylisoquinoline, was developed and investigated for excited-state electron transfer with sacrificial electron donors that included triethanolamine (TEOA), triethylamine (TEA) and 1,3-dimethyl-2-phenyl-2,3-dihydro-1*H*-benzo[*d*]imidazole (BIH) in acetonitrile. The photosensitizers were obtained in 57–82% yield starting from the common [Ir(piq)$_2$μ-Cl]$_2$ precursor and were all characterized by UV–Vis absorption as well as by steady-state, time-resolved spectroscopies and electrochemistry. The excited-state lifetimes ranged from 250 to 3350 ns and excited-state electron transfer quenching rate constants in the 10^9 M^{-1} s^{-1} range were obtained when BIH was used as electron donor. These quenching rate constants were three orders of magnitude higher than when TEA or TEOA was used. Steady-state photolysis in the presence of BIH showed that the stable and reversible accumulation of mono-reduced photosensitizers was possible, highlighting the potential use of these Ir-based photosensitizers in photocatalytic reactions relevant for solar fuels production.

1 Introduction

The global population has recently reached 7.9 billion, and energy demand increases commensurately. It is nowadays accepted that fossil fuels alone will not be sufficient to provide both the energy and chemical feedstocks required over the years to come. The necessity for renewable sources of energy and feedstock is therefore at an unprecedented high, and the energy provided by the sun has long been viewed as the ideal candidate [1–4]. Light-driven energy conversion was proposed as an alternative to fossil fuels already more than a century ago by Giacomo Ciamician, who urged society to make better use of radiant energy through photoinduced chemical reactions [5].

Both natural and artificial photosynthesis aim to generate high-energy fuels using sunlight to initiate a series of light-induced electron transfer events [6–12]. Visible light induced electron transfer chemistry, reminiscent of photosynthesis, represents a powerful approach towards the development of sustainable energy supplies. In this context, the reduction of protons into molecular hydrogen (H_2) or of CO_2 into valuable chemicals such as CO, HCOOH, CH_3OH or CH_4 are both considered as promising strategies towards sustainability [13–23]. Research has been dedicated to the development of transition metal complexes that function as photosensitizers as well as catalytic centers where these reduction processes could take place. Prototypical photosensitizers such as [Ru(bpy)$_3$]$^{2+}$ (bpy = 2,2′-bipyridine) and [Ir(ppy)$_3$] (ppy = 2-phenylpyridine) have been used in concert with Ni, Ru, Re, Fe and Co based molecular catalysts for proton or CO_2 reduction [13–23]. Typically, visible light excitation of the photosensitizer leads to an excited state that undergoes direct electron transfer with a sacrificial electron donor. Commonly used sacrificial electron donors include triethanolamine (TEOA) or 1,3-dimethyl-2-phenyl-2,3-dihydro-1*H*-benzo[*d*]imidazole (BIH) with formal reduction potentials of 0.57–0.82 V vs. SCE and 0.33 V vs. SCE, respectively [24]. The monoreduced photosensitizer

Martin Wodon, Simon De Kreijger have contributed equally to this work.

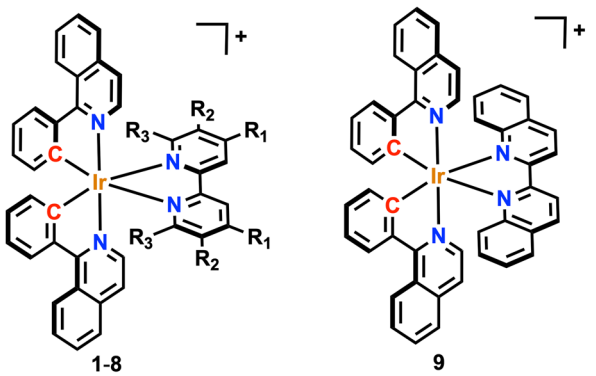
✉ Benjamin Elias
Benjamin.Elias@uclouvain.be

✉ Ludovic Troian-Gautier
Ludovic.Troian@uclouvain.be

[1] Université catholique de Louvain (UCLouvain), Institut de la Matière Condensée et des Nanosciences (IMCN), Molecular Chemistry, Materials and Catalysis (MOST), Place Louis Pasteur 1, bte L4.01.02, 1348 Louvain-la-Neuve, Belgium

[2] Department of Chemistry, University of North Carolina at Chapel Hill, Chapel Hill 27599-3290, USA

Published online: 20 May 2022



$[Ir(piq)_2(bpy)]^+$ (**1**): $R_1 = R_2 = R_3 = H$
$[Ir(piq)_2(4,4'\text{-}(CH_3)_2\text{-bpy})]^+$ (**2**): $R_1 = CH_3$, $R_2 = R_3 = H$
$[Ir(piq)_2(5,5'\text{-}(CH_3)_2\text{-bpy})]^+$ (**3**): $R_1 = H$, $R_2 = CH_3$, $R_3 = H$
$[Ir(piq)_2(6,6'\text{-}(CH_3)_2\text{-bpy})]^+$ (**4**): $R_1 = R_2 = H$, $R_3 = CH_3$
$[Ir(piq)_2(4,4'\text{-}(^t Bu)_2\text{-bpy})]^+$ (**5**): $R_1 = {}^t Bu$, $R_2 = R_3 = H$
$[Ir(piq)_2(4,4'\text{-}(C_9H_{19})_2\text{-bpy})]^+$ (**6**): $R_1 = (CH_2)_8CH_3$ $R_2 = R_3 = H$
$[Ir(piq)_2(4,4'\text{-}(OCH_3)_2\text{-bpy})]^+$ (**7**): $R_1 = OCH_3$, $R_2 = R_3 = H$
$[Ir(piq)_2(4,4'\text{-}(Br)_2\text{-bpy})]^+$ (**8**): $R_1 = Br$, $R_2 = R_3 = H$
$[Ir(piq)_2(biq)]^+$ (**9**): biq = 2,2'-biquinoline

Fig. 1 The series of $[Ir(piq)_2(LL)]^+.PF_6^-$ photosensitizers investigated in the present work

is then able to transfer an electron to a molecular catalyst, commonly $[Co(dmgH)_2(py)(Cl)]$ ($E_{Co(III)/Co(II)} = -0.65$ V and $E_{Co(II)/Co(I)} = -1.02$ V *vs.* SCE) [25] for proton reduction or [*fac*-$Re(bpy)(CO)_3Cl$] ($E_{bpy/bpy-} = -1.35$ V and $E_{Re(I)/Re(0)} = -1.71$ V vs. SCE) [26] for CO_2 reduction.

This sequence of reductive electron transfer events relies on a delicate balance of thermodynamics, and fine-tuning the ground- and excited-state energy levels of the photosensitizers is essential for efficient process. In this context, bis-cyclometalated Ir(III) complexes are particularly useful, as the significant spatial separation of each frontier orbital enables independent tuning of either the HOMO or the LUMO of the complex (or both) [27, 28]. In addition, Ir(III) photosensitizer are often very robust under irradiation and their (photo)-redox potentials can be tuned over a far greater range than their Ru(II), Os(II) or Cu(I) counterparts. [28, 29].

In here, we report a series of nine $[Ir(piq)_2(LL)]^+$ photosensitizers, where piqH = 1-phenylisoquinoline and LL is a N^N diimine ligand (Fig. 1). These photosensitizers absorbed visible light with molar absorption coefficients in the 5400–7900 M^{-1} cm^{-1} range, and exhibit excited-state lifetimes in the microsecond time scales that were competent for efficient reductive excited-state electron transfer with BIH. Steady-state photolysis in the presence of BIH showed that most of the photosensitizers were stable in their reduced form, which is a paramount criterion for efficient and long-term light-driven reduction of protons or CO_2 to solar fuel products.

2 Experimental

Electrochemistry Cyclic voltammetry was performed with an Autolab PGSTAT 100 potentiostat using a standard three-electrode-cell, i.e. a glassy carbon disk working electrode (approximate area = 0.03 cm^2), a platinum wire counter electrode and an aqueous Ag/AgCl reference electrode (salt bridge: 3 M KCl/saturated AgCl). Experiments were performed in dry 0.1 M tetrabutylammonium hexafluorophosphate acetonitrile electrolyte, and the samples were purged with argon before each measurement.

Stern–Volmer experiments Excited-state quenching experiments were performed on a Varian Cary Eclipse spectrometer and the photoluminescence spectra were not corrected for the instrument's response. Typically, an Ir (III) solution with an absorbance of ~ 0.1 around 420–440 nm was prepared in acetonitrile. Various quencher solutions with concentration ranging from 0.05 to 0.5 M were prepared in the desired solvent also containing the Ir(III) photosensitizer with the same absorbance. The solutions were purged with argon for 30 min prior to the experiments and UV–Vis measurements were performed to ensure constant concentration throughout the entire measurement. The desired quencher was gradually added to the solution of iridium photosensitizer and the excited-state quenching was monitored by steady-state photoluminescence. The decrease of photoluminescence was related to the concentration of quencher and the respective Stern–Volmer plots were extrapolated using the following equation:

$$\frac{\sum (PLI_0)}{\sum (PLI)} = 1 + K_{SV}[Q] = 1 + k_q \tau_0 [Q].$$

Transient absorption Nanosecond transient absorption measurements were recorded on a LP920-K spectrometer from Edinburgh Instruments equipped with an iCCD detector from Andor. The excitation source was a tunable Nd:YAG Laser NT342 Series from EKSPLA. The third harmonic (355 nm) at 150 mJ was directed into an optical parametric oscillator (OPO) to enable wavelength tuning starting from 410 nm. The laser power was then attenuated to reach appreciable signal/noise (typically 10 mJ/pulse) and the integrity of the samples was verified by UV–Vis measurements. All samples were recorded in argon-purged acetonitrile at room temperature.

Synthesis of the Ir(III) photosensitizers Ir(III) chloro-bridged dimer $[Ir(piq)_2\mu\text{-}Cl]_2$ (75 mg, 58.9 µmol) and the corresponding diimine ligand (147.25 µmol, 2.5 eq.) were placed in a sealed tube under argon atmosphere with 9 mL of MeOH/DCM 2:1 mixture. The reaction was heated at 60 °C for 24 h. After reaction, the orange-red mixture was brought to room temperature. The DCM fraction was evaporated, and the resulting solution was treated with 10 mL of milliQ

water and an excess of NH_4PF_6 was then added. The complex was isolated by centrifugation and was washed 3 times with milliQ water and 3 times with diethyl ether to give the desired complexes with yields that ranged from 57 to 82%.

$[Ir(piq)_2(bpy)]^+.PF_6^-$ was obtained using the synthetic procedure described above with 2,2′-bipyridine as diimine ligand (23 mg), to give an orange powder (84.8 mg, 80% yield). **^{1}H NMR** (500 MHz, CD_3CN) δ 9.04–8.99 (m, 2H), 8.54 (d, J = 8.2 Hz, 2H), 8.38 (d, J = 8.1 Hz, 2H), 8.11 (td, J = 7.9, 1.6 Hz, 2H), 8.04–7.92 (m, 2H), 7.87 (ddd, J = 5.5, 1.6, 0.8 Hz, 2H), 7.85–7.78 (m, 4H), 7.51 (d, J = 6.4 Hz, 2H), 7.46 (ddd, J = 7.7, 5.5, 1.2 Hz, 2H), 7.42 (dd, J = 6.5, 0.9 Hz, 2H), 7.18–7.05 (m, 2H), 6.88 (td, J = 7.4, 1.3 Hz, 2H), 6.31 (dd, J = 7.6, 1.3 Hz, 2H). **HRMS** (ESI) *m/z* calculated for $[C_{40}H_{28}N_4Ir–PF_6]^+$ = 755.19144; found 755.19152. NMR data are consistent with literature values. [30].

$[Ir(piq)_2(4,4'\text{-}(CH_3)_2\text{-}bpy)]^+.PF_6^-$ was obtained using the synthetic procedure described above with 4,4′-dimethyl-2,2′-bipyridine as diimine ligand (27.1 mg), to give an orange powder (88.1 mg, 80% yield). **^{1}H NMR** (500 MHz, CD_3CN) δ 9.06–8.95 (m, 2H), 8.44–8.27 (m, 4H), 8.06–7.92 (m, 2H), 7.91–7.74 (m, 4H), 7.68 (d, J = 5.7 Hz, 2H), 7.50 (d, J = 6.4 Hz, 2H), 7.42 (dd, J = 6.5, 0.9 Hz, 2H), 7.28 (ddd, J = 5.6, 1.8, 0.8 Hz, 2H), 7.12 (ddd, J = 8.2, 7.3, 1.3 Hz, 2H), 6.87 (td, J = 7.4, 1.3 Hz, 2H), 6.32–6.30 (m, 2H), 2.51 (s, 6H). **HRMS** (ESI) *m/z* calculated for $[C_{42}H_{32}N_4Ir–PF_6]^+$ = 783.22274; found 783.22266. NMR data are consistent with literature values [31].

$[Ir(piq)_2(5,5'\text{-}(CH_3)_2\text{-}bpy))]^+.PF_6^-$ was obtained using the synthetic procedure described above with 5,5′-dimethyl-2,2′-bipyridine as diimine ligand (27.1 mg), to give an orange powder (78.1 mg, 71% yield). **^{1}H NMR** (500 MHz, CD_3CN) δ 9.08–8.98 (m, 2H), 8.37 (t, J = 8.1 Hz, 4H), 8.04–7.96 (m, 2H), 7.93–7.88 (m, 2H), 7.87–7.77 (m, 4H), 7.60 (d, J = 2.0 Hz, 2H), 7.51 (d, J = 6.4 Hz, 2H), 7.42 (d, J = 6.4 Hz, 2H), 7.13 (ddd, J = 8.3, 7.2, 1.4 Hz, 2H), 6.88 (td, J = 7.4, 1.3 Hz, 2H), 6.30 (dd, J = 7.7, 1.3 Hz, 2H), 2.14 (s, 6H). **HRMS** (ESI) *m/z* calculated for $[C_{42}H_{32}N_4Ir–PF_6]^+$ = 783.22274; found 783.22251. NMR data are consistent with literature values [32].

$[Ir(piq)_2(6,6'\text{-}(CH_3)_2\text{-}bpy))]^+.PF_6^-$ was obtained using the synthetic procedure described above with 6,6´-dimethyl-2,2´-bipyridine as diimine ligand (27.1 mg), to give an orange powder (84.3 mg, 77% yield). **^{1}H NMR** (500 MHz, CD_3CN) δ 9.01–8.89 (m, 2H), 8.29 (d, J = 7.5 Hz, 2H), 8.19 (d, J = 8.0 Hz, 2H), 8.04–7.97 (m, 2H), 7.91 (t, J = 7.9 Hz, 2H), 7.88–7.75 (m, 6H), 7.45 (d, J = 6.2 Hz, 2H), 7.29 (dd, J = 7.7, 1.2 Hz, 2H), 7.03 (ddd, J = 8.3, 7.2, 1.3 Hz, 2H), 6.81–6.61 (m, 2H), 6.30 (dd, J = 7.7, 1.3 Hz, 2H), 1.81 (s, 6H). **HRMS** (ESI) *m/z* calculated for $[C_{42}H_{32}N_4Ir–PF_6]^+$ = 783.22274; found 783.22256.

$[Ir(piq)_2(4,4'\text{-}(^tBu)_2\text{-}bpy))]^+.PF_6^-$ was obtained using the synthetic procedure described above with 4,4'-^{t}Bu-2,2′-bipyridine as diimine ligand (39.5 mg), to give an orange powder (68.6 mg, 57% yield). **^{1}H NMR** (500 MHz, CD_3CN) δ 9.07–8.95 (m, 2H), 8.52 (dd, J = 2.1, 0.7 Hz, 2H), 8.37 (d, J = 8.0 Hz, 2H), 8.08–7.93 (m, 2H), 7.89–7.79 (m, 4H), 7.73 (dd, J = 5.9, 0.6 Hz, 2H), 7.55–7.36 (m, 6H), 7.12 (ddd, J = 8.1, 7.2, 1.3 Hz, 2H), 6.87 (td, J = 7.4, 1.2 Hz, 2H), 6.30 (dd, J = 8.0, 1.3 Hz, 2H), 1.39 (s, 18H). **HRMS** (ESI) *m/z* calculated for $[C_{48}H_{44}N_4Ir–PF_6]^+$ = 867.31664; found 867.31621. NMR data are consistent with literature values [33].

$[Ir(piq)_2(4,4'\text{-}(C_9H_{19})_2\text{-}bpy))]^+.PF_6^-$ was obtained using the synthetic procedure described above with 4,4′-$CH_3(CH_2)_8$-2,2′-bipyridine as diimine ligand (60.1 mg), to give an orange powder (81.3 mg, 60% yield). **^{1}H NMR** (500 MHz, CD_3CN) δ 9.01 (dd, J = 6.4, 3.4 Hz, 2H), 8.48–8.30 (m, 4H), 8.07–7.93 (m, 2H), 7.90–7.74 (m, 4H), 7.69 (d, J = 5.9 Hz, 2H), 7.49 (d, J = 6.5 Hz, 2H), 7.42 (d, J = 5.9 Hz, 2H), 7.28 (dd, J = 5.7, 1.9 Hz, 2H), 7.17–7.05 (m, 2H), 6.87 (td, J = 7.4, 1.3 Hz, 2H), 6.31 (dd, J = 7.7, 1.4 Hz, 2H), 2.78 (t, J = 7.7 Hz, 4H), 1.69 (q, J = 7.2 Hz, 4H), 1.45–1.09 (m, 24H), 0.99–0.68 (m, 6H). **HRMS** (ESI) *m/z* calculated for $[C_{58}H_{64}N_4Ir–PF_6]^+$ = 1007.47314; found 1007.47317. NMR data are consistent with literature values [34].

$[Ir(piq)_2(4,4'\text{-}(OCH_3)_2\text{-}bpy)]^+.PF_6^-$ was obtained using the synthetic procedure described above with 4,4′-MeO-2,2′-bipyridine as diimine ligand (31.8 mg), to give an orange powder (93.4 mg, 82% yield). **^{1}H NMR** (500 MHz, CD_3CN) δ 9.07–8.92 (m, 2H), 8.36 (d, J = 8.0 Hz, 2H), 8.00 (dd, J = 6.8, 2.7 Hz, 4H), 7.92–7.72 (m, 4H), 7.61 (d, J = 6.4 Hz, 2H), 7.56 (d, J = 6.5 Hz, 2H), 7.45 (d, J = 6.3 Hz, 2H), 7.16–7.06 (m, 2H), 6.98 (dd, J = 6.4, 2.7 Hz, 2H), 6.86 (td, J = 7.4, 1.3 Hz, 2H), 6.31 (dd, J = 7.9, 1.1 Hz, 2H), 3.97 (s, 6H). **HRMS** (ESI) *m/z* calculated for $[C_{42}H_{32}O_2N_4Ir–PF_6]^+$ = 815.21257; found 815.21250. NMR data are consistent with literature values [35].

$[Ir(piq)_2(4,4'\text{-}(Br)_2\text{-}bpy)]^+.PF_6^-$ was obtained using the synthetic procedure described above with 4,4′-Br-2,2′-bipyridine as diimine ligand (45.9 mg), to give a red powder (86.3 mg, 70% yield). **^{1}H NMR** (500 MHz, CD_3CN) δ 9.08–8.95 (m, 2H), 8.79 (dd, J = 1.7, 0.9 Hz, 2H), 8.52–8.29 (m, 2H), 8.04–7.97 (m, 2H), 7.90–7.79 (m, 4H), 7.66 (t, J = 1.1 Hz, 4H), 7.51 (d, J = 6.4 Hz, 2H), 7.48–7.42 (m, 2H), 7.13 (ddd, J = 8.2, 7.3, 1.3 Hz, 2H), 6.88 (td, J = 7.5, 1.3 Hz, 2H), 6.26 (dd, J = 7.7, 1.3 Hz, 2H). **HRMS** (ESI) *m/z* calculated for $[C_{40}H_{26}N_4Br_2Ir–PF_6]^+$ = 911.01246; found 911.01276.

$[Ir(piq)_2(biq)]^+.PF_6^-$ was obtained using the synthetic procedure described above with 2,2′-biquinoline as diimine ligand (37.7 mg), to give a dark purple

powder (96.2 mg, 81% yield). **^{1}H NMR** (500 MHz, CD_3CN) δ 8.82 (d, $J = 8.8$ Hz, 2H), 8.65 (d, $J = 8.7$ Hz, 2H), 8.56 (d, $J = 8.8$ Hz, 2H), 8.27 (d, $J = 7.4$ Hz, 2H), 8.00–7.89 (m, 4H), 7.86–7.70 (m, 8H), 7.53 (ddd, $J = 8.1$, 6.8, 1.1 Hz, 2H), 7.31 (d, $J = 6.5$ Hz, 2H), 7.14 (ddd, $J = 8.7$, 6.8, 1.5 Hz, 2H), 7.10 (ddd, $J = 8.2$, 7.2, 1.3 Hz, 2H), 6.87 (td, $J = 7.4$, 1.3 Hz, 2H), 6.47 (dd, $J = 7.8$, 1.4 Hz, 2H). **HRMS** (ESI) m/z calculated for $[C_{48}H_{32}N_4Ir–PF_6]^+ = 855.22274$; found 855.22281. NMR data are consistent with literature values [36].

3 Results and discussions

The synthetic approach to produce the series of iridium(III) photosensitizers relied on the use of iridium complexes with two cyclometalating piq ligands (piqH = 1-phenylisoquinoline). These ligands are relatively electron-rich and are also known to increase the molar absorption coefficient of the resulting photosensitizers in the visible range [28]. The synthesis proceeded via the chelation of the cyclometalated ligands (providing an Ir(III) dichloro-bridged dimer), as described by Nonoyama [37], followed by the addition of the N^N ligand. The N^N ligands were systematically varied over a wide range of ligand substitutions, which included 2,2′-bipyridine (bpy), 4,4′-, 5,5′, and 6,6´-$(CH_3)_2$-2,2′-bipyridine, 4,4′-$(OCH_3)_2$-2,2′-bipyridine, 4,4′-$(^tBu)_2$-2,2′-bipyridine, 4,4′-$(C_9H_{19})_2$-2,2′-bipyridine, 4,4′-$(Br)_2$-2,2′-bipyridine as well as 2,2′-biquinoline (biq). The modifications of the N^N diimine ligands influenced the LUMO energy level of each complex, which in turn affected the visible light absorption properties, as well as the ground-state and excited-state reduction potentials, $E_{1/2}(Ir^{+*/0})$.

The UV–visible absorption features of all complexes were characterized by strong ligand-centered (LC) absorption bands in the UV region (Fig. 2). The transitions observed at wavelengths greater than 350 nm are often assigned to mixed metal-to-ligand (MLCT) and ligand-to-ligand (LLCT) charge transfer bands as well as metal–ligand-to-ligand charge transfer (MLLCT) from the Ir-Cyclometalating ligand fragment to the N^N ligand [28, 38, 39]. These transitions were determined to have molar absorption coefficients in the 5400–7900 M^{-1} cm^{-1} range at 427–442 nm (Table 1).

Blue light excitation yielded photoluminescence (PL) decays that were in all cases well described using a bi-exponential decay. Independent of the nature of the photosensitizer, a short excited-state lifetime (15 ± 2 ns) was determined in all cases, which is tentatively assigned as radiative decay from piq-centered excited states. The second component of the excited-state lifetime, tabulated in Table 1, was strongly influenced by the nature of the N^N ligand, where electron withdrawing groups such as in 4,4′-$(Br)_2$-2,2′-bipyridine and 2,2′-biquinoline exhibited shorter excited-state lifetimes (τ) of 250 and 313 ns, respectively, while photosensitizers bearing more electron-rich ligands exhibited lifetimes values between 1.41 µs and 3.35 µs, (Table 1).

The photoluminescence quantum yields (ϕ_{PL}), under air and in argon-purged solutions, were determined by comparative actinometry (Eq. 1) using $[Ru(bpy)_3]^{2+}$ as the actinometer (act) [40]. In Eq. 1, PL refers to the integrated photoluminescence spectra, A to the absorbance of the solution at the excitation wavelength, and η to the refractive index of the solvent. $[Ir(piq)_2(4,4'\text{-}(Br)_2\text{-bpy})]^+$ and $[Ir(piq)_2(biq)]^+$ each exhibited a moderate ϕ_{PL} of 0.029 and 0.063 under argon, respectively. All other photosensitizers exhibited a ϕ_{PL} between 0.108 and 0.161 under argon. For the photosensitizers with τ greater than 1 µs, ϕ_{PL} was always 4 to 6 times greater under argon than under air, indicating the possibility of quenching via $^1O_2$ photosensitization. Quenching rate constant by triplet oxygen of $(2–7) \times 10^8$ M^{-1} s^{-1} for those photosensitizers were estimated using an oxygen concentration of 2.4 mM for the air-saturated acetonitrile [41].

$$\phi_{PL}^{PS} = \left(\phi_{PL}^{Act}\right)\left(\frac{PL^{PS}}{PL^{Act}}\right)\left(\frac{1-10^{-A^{Act}}}{1-10^{-A^{PS}}}\right)\left(\frac{\eta_{PS}^2}{\eta_{Act}^2}\right). \quad (1)$$

The iridium photosensitizers were also characterized by differential pulse voltammetry (DPV) (Fig. 3), as well as by cyclic voltammetry (Figs. S1–S9) in 0.1 M $TBAPF_6$ CH_3CN electrolytes. The nine photosensitizers exhibited reversible $Ir^{IV/III}$ reduction waves at potentials centered between 1.21 and 1.33 V vs NHE. The introduction of electron-withdrawing derivatives, such as 4,4′-$(Br)_2$-2,2′-bipyridine and 2,2′-biquinoline had little influence on the $Ir^{IV/III}$ redox couple. On the other hand, the ligand-centered reductions were strongly influenced by the nature of the substituents on the 2,2′-bipyridine backbone. Compared to $[Ir(piq)_2(bpy)]^+$, which displayed a first one-electron ligand-centered reduction at – 1.35 V vs NHE, derivatives with electron donating substituents in the 4,4′, 5,5′ or 6,6´ position shifted the reduction potentials 60–120 mV more negative. The introduction of 4,4′-$(C_9H_{19})_2$-2,2′-bipyridine resulted in a 10 mV anodic shift compared to the prototypical $[Ir(piq)_2(bpy)]^+$. The most drastic shifts were observed for the photosensitizers bearing 4,4′-$(Br)_2$-2,2′-bipyridine and 2,2′-biquinoline ligands, where the ligand-centered reductions were shifted by + 320 mV and + 410 mV, respectively. The corresponding excited-state reduction (E_{red}*) and oxidation (E_{ox}*) potentials were determined using Eqs. 2 and 3, where E_{00} corresponds to the free energy stored in the excited state [42, 43]. As expected based on ground-state reduction potentials, $[Ir(piq)_2(4,4'\text{-}(Br)_2\text{-bpy})]^+$ and $[Ir(piq)_2(biq)]^+$ were the

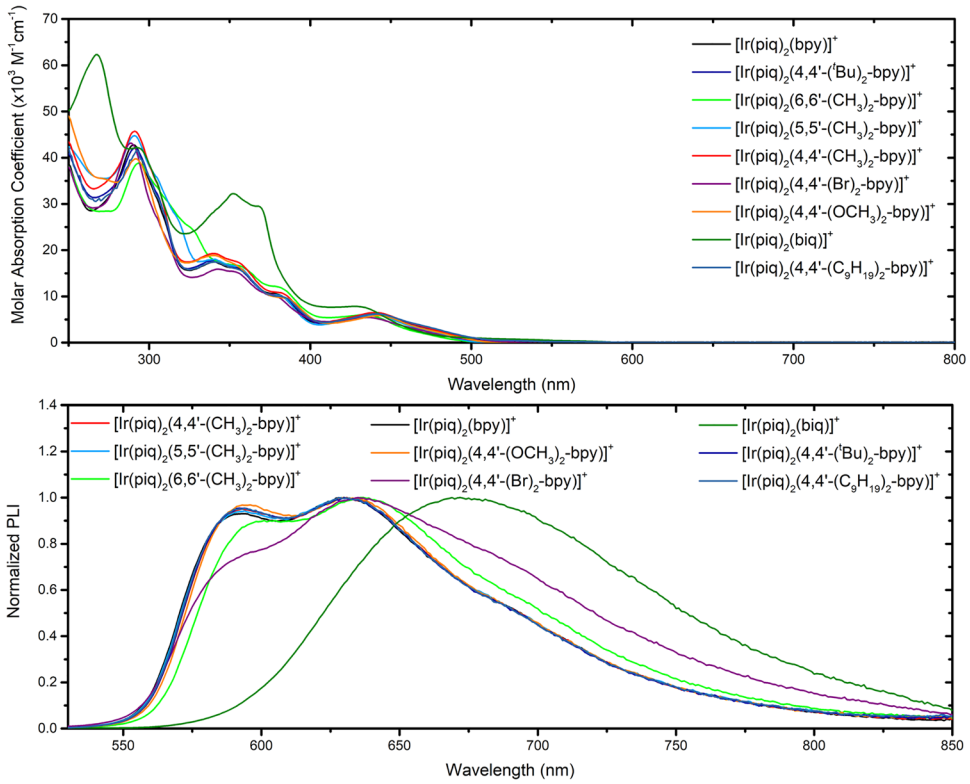


Fig. 2 UV–Visible absorption (top) and photoluminescence (bottom) spectra of $[Ir(piq)_2(bpy)]^+$ (black), $[Ir(piq)_2(4,4'\text{-}(^tBu)_2\text{-bpy})]^+$ (blue), $[Ir(piq)_2(6,6'\text{-}(CH_3)_2\text{-bpy})]^+$ (green), $[Ir(piq)_2(5,5'\text{-}(CH_3)_2\text{-bpy})]^+$ (light blue), $[Ir(piq)_2(4,4'\text{-}(CH_3)_2\text{-bpy})]^+$ (red), $[Ir(piq)_2(4,4'\text{-}(Br)_2\text{-bpy})]^+$ (purple), $[Ir(piq)_2(4,4'\text{-}(OCH_3)_2\text{-bpy})]^+$ (orange), $[Ir(piq)_2(biq)]^+$ (olive) and $[Ir(piq)_2(4,4'\text{-}(C_9H_{19})_2\text{-bpy})]^+$ (pale blue) recorded in acetonitrile at room temperature under argon

Table 1 Photophysical properties of photosensitizers **1–9** recorded in acetonitrile under argon

Compound	Abs (ε)	PL_{max}	τ (ns)	ϕ^a	k_r ($\times 10^4 s^{-1}$)	k_{nr} ($\times 10^6 s^{-1}$)
$[Ir(piq)_2(bpy)]^+$ (1)	438 (6300)	630, 594	2580	0.108 (0.024)	4.84	0.34
$[Ir(piq)_2(4,4'\text{-}(CH_3)_2\text{-bpy})]^+$ (2)	440 (6500)	631, 593	3210	0.143 (0.025)	4.76	0.26
$[Ir(piq)_2(5,5'\text{-}(CH_3)_2\text{-bpy})]^+$ (3)	440 (6000)	629, 594	3160	0.151 (0.024)	4.83	0.27
$[Ir(piq)_2(6,6'\text{-}(CH_3)_2\text{-bpy})]^+$ (4)	434 (6000)	637, 601	3350	0.143 (0.027)	4.20	0.26
$[Ir(piq)_2(4,4'\text{-}(^tBu)_2\text{-bpy})]^+$ (5)	441 (5900)	630, 594	1410	0.145 (0.022)	10.6	0.60
$[Ir(piq)_2(4,4'\text{-}(C_9H_{19})_2\text{-bpy})]^+$ (6)	441 (6200)	630, 592	3180	0.137 (0.053)	4.31	0.27
$[Ir(piq)_2(4,4'\text{-}(OCH_3)_2\text{-bpy})]^+$ (7)	442 (5900)	630, 596	2960	0.161 (0.030)	5.52	0.28
$[Ir(piq)_2(4,4'\text{-}(Br)_2\text{-bpy})]^+$ (8)	436 (5400)	635	250	0.029 (0.020)	12.1	3.88
$[Ir(piq)_2(biq)]^+$ (9)	427 (7900)	669	313	0.063 (0.044)	20.4	2.99

[a]Values for air-equilibrated solution in parenthesis

most potent photo-oxidants, with E_{red}* of 1.41 and 1.37 V vs NHE, respectively. The other 7 photosensitizers had very similar E_{red}* (Table 2).

$$E^*_{red} = E_{1/2}\left(Ir^{*(0/-)}\right) = E_{1/2}\left(L^{n/n-1}\right) + E_{00} \quad (2)$$

$$E^*_{ox} = E_{1/2}\left(Ir^{*(+/0)}\right) = E_{1/2}\left(Ir^{IV/III}\right) - E_{00} \quad (3)$$

Excited-state reactivity of all $[Ir(piq)_2(LL)]^+$ photosensitizers towards TEA, TEOA and BIH as sacrificial electron donors was investigated in argon-purged acetonitrile. The driving force for electron transfer with BIH, TEOA and TEA was estimated based on available ground and excited-state reduction potentials. With BIH as sacrificial electron donor, the driving force for electron transfer from all complexes was exergonic, with the Gibbs free energy for electron transfer, ΔG, ranging from – 0.39 eV for $[Ir(piq)_2(4,4'\text{-}(OCH_3)_2\text{-bpy})]^+$ to – 0.83 eV for $[Ir(piq)_2(4,4'\text{-}(Br)_2\text{-bpy})]^+$. With TEA and TEOA as the electron donors, ΔG was almost always ergoneutral or slightly endergonic. From the tabulated values in Table 3, ΔG became more exergonic with

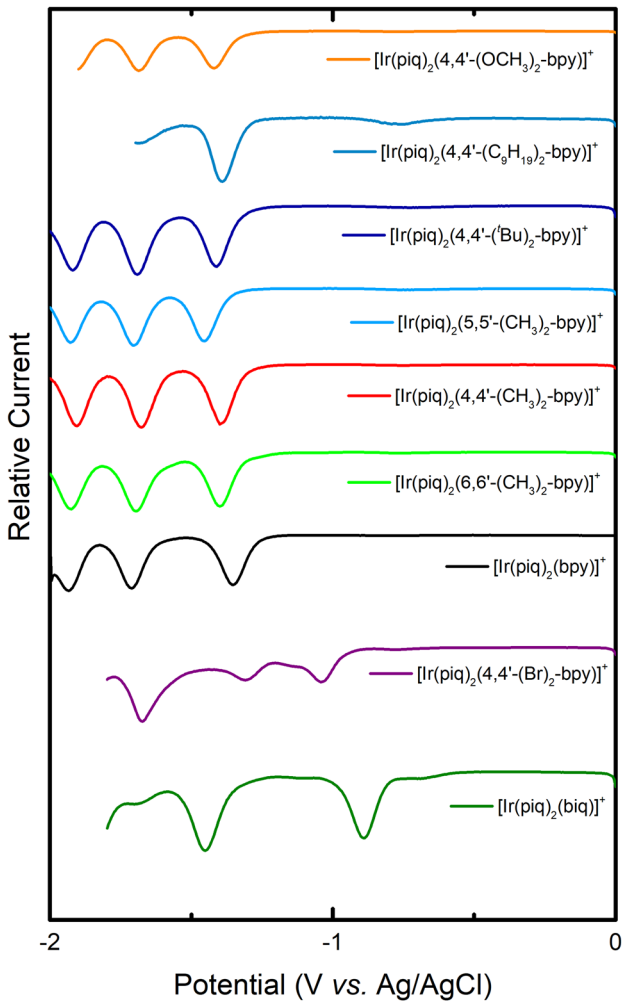


Fig. 3 Differential pulse voltammetry of $[Ir(piq)_2(bpy)]^+$ (black), $[Ir(piq)_2(4,4'\text{-}(^tBu)_2\text{-}bpy)]^+$ (blue), $[Ir(piq)_2(6,6'\text{-}(CH_3)_2\text{-}bpy)]^+$ (green), $[Ir(piq)_2(5,5'\text{-}(CH_3)_2\text{-}bpy)]^+$ (light blue), $[Ir(piq)_2(4,4'\text{-}(CH_3)_2\text{-}bpy)]^+$ (red), $[Ir(piq)_2(4,4'\text{-}(Br)_2\text{-}bpy)]^+$ (purple), $[Ir(piq)_2(4,4'\text{-}(OCH_3)_2\text{-}bpy)]^+$ (orange), $[Ir(piq)_2(biq)]^+$ (olive) and $[Ir(piq)_2(4,4'\text{-}(C_9H_{19})_2\text{-}bpy)]^+$ (pale blue) recorded in 0.1 M $TBAPF_6$ acetonitrile electrolyte at room temperature

more potent photo-oxidants, i.e. $[Ir(piq)_2(4,4'\text{-}(Br)_2\text{-}bpy)]^+$ and $[Ir(piq)_2(biq)]^+$. This observation was also evident from Stern–Volmer measurements (Figs. 4 and S10–S17). A representative result of a Stern–Volmer titration using $[Ir(piq)_2(6,6'\text{-}(CH_3)_2\text{-}bpy)]^+$ with BIH, TEA and TEOA as the electron donors is shown in Fig. 4. With BIH, drastic quenching of the steady-state photoluminescence was observed. The corresponding Stern–Volmer plot was linear within the quencher concentration range examined. From the slope, and taking the longest value of τ, a quenching rate constant (k_q) of 5.3×10^9 M^{-1} s^{-1} was determined. With TEA and TEOA, only moderate excited-state quenching was observed and the corresponding Stern–Volmer plots exhibited a downward curvature. This downward curvature was observed for almost all of the iridium(III) photosensitizers investigated in this study. Although a corresponding quenching rate constant could not be unambiguously determined, Fig. 4h indicates that the excited-state quenching was approximately three orders of magnitude smaller (10^6 M^{-1} s^{-1}) than with BIH. To gain additional information of this peculiar behavior, we performed time-resolved quenching experiments using $[Ir(piq)_2(bpy)]^+$ and TEA. Excited-state quenching was unambiguously observed when the concentration of TEA was gradually increased to 1.32 M. The corresponding Stern–Volmer plot was linear and the corresponding quenching rate constant of 7.1×10^5 M^{-1} s^{-1} was determined from the slope. (Fig. S18) This experiment confirmed the greater excited-state quenching conferred by BIH compared to TEA. The Stern–Volmer plots for the excited-state quenching of the nine Ir(III) photosensitizers with BIH are shown in Fig. 4i. The Stern–Volmer plots were all linear and the corresponding quenching rate constants were determined in the range of 1.6×10^9 M^{-1} s^{-1} to 7.1×10^9 M^{-1} s^{-1} (Table 3). These quenching rate constants were in line with other reports using iridium(III) PS and BIH electron donor [46, 47]. A rather counterintuitive quenching behavior was noted for photosensitizers $[Ir(piq)_2(4,4'\text{-}(Br)_2\text{-}bpy)]^+$ and

Table 2 Ground and excited-state reduction potentials for photosensitizers **1–9**

Complex	$E_{1/2}(Ir^{IV/III})$ V vs NHE	$E_{1/2}(L^{n/n-1})$ V vs NHE	E_{00} (eV)[a]	E_{ox}* V vs NHE	E_{red}* V vs NHE
$[Ir(piq)_2(bpy)]^+$ (1)	1.28	– 1.35	2.23	– 0.75	1.08
$[Ir(piq)_2(4,4'\text{-}(CH_3)_2\text{-}bpy)]^+$ (2)	1.25	– 1.43	2.23	– 0.78	0.99
$[Ir(piq)_2(5,5'\text{-}(CH_3)_2\text{-}bpy)]^+$ (3)	1.28	– 1.47	2.23	– 0.75	0.96
$[Ir(piq)_2(6,6'\text{-}(CH_3)_2\text{-}bpy)]^+$ (4)	1.25	– 1.42	2.21	– 0.77	0.99
$[Ir(piq)_2(4,4'\text{-}(^tBu)_2\text{-}bpy)]^+$ (5)	1.26	– 1.41	2.23	– 0.77	1.02
$[Ir(piq)_2(4,4'\text{-}(C_9H_{19})_2\text{-}bpy)]^+$ (6)	1.27	– 1.34	2.23	– 0.76	1.01
$[Ir(piq)_2(4,4'\text{-}(OCH_3)_2\text{-}bpy)]^+$ (7)	1.24	– 1.46	2.22	– 0.78	0.96
$[Ir(piq)_2(4,4'\text{-}(Br)_2\text{-}bpy)]^+$ (8)	1.33	– 1.03	2.24	– 0.71	1.41
$[Ir(piq)_2(biq)]^+$ (9)	1.21	– 0.94	2.11	– 0.70	1.37

[a]The E_{00} was determined using the generalizable method of extrapolating a tangent line on the blue edge of the corrected PL spectrum to the emission baseline [44, 45].

Table 3 Driving force (ΔG) and quenching rate constants (k_q) for electron transfer between BIH, TEOA or TEA and excited photosensitizers **1–9**

Compound	ΔG_{BIH} (eV)	ΔG_{TEOA} (eV)	ΔG_{TEA} (eV)	k_q (BIH) (M^{-1} s^{-1})
$[Ir(piq)_2(bpy)]^+$ (1)	− 0.51	0.00	− 0.06	7.1×10^9
$[Ir(piq)_2(4,4'\text{-}(CH_3)_2\text{-}bpy)]^+$ (2)	− 0.42	0.09	0.03	3.7×10^9
$[Ir(piq)_2(5,5'\text{-}(CH_3)_2\text{-}bpy)]^+$ (3)	− 0.39	0.12	0.06	3.8×10^9
$[Ir(piq)_2(6,6'\text{-}(CH_3)_2\text{-}bpy)]^+$ (4)	− 0.42	0.09	0.03	5.3×10^9
$[Ir(piq)_2(4,4'\text{-}(^tBu)_2\text{-}bpy)]^+$ (5)	− 0.44	0.06	0.00	5.1×10^9
$[Ir(piq)_2(4,4'\text{-}(C_9H_{19})_2\text{-}bpy)]^+$ (6)	− 0.44	0.07	0.01	2.4×10^9
$[Ir(piq)_2(4,4'\text{-}(OCH_3)_2\text{-}bpy)]^+$ (7)	− 0.39	0.12	0.06	2.9×10^9
$[Ir(piq)_2(4,4'\text{-}(Br)_2\text{-}bpy)]^+$ (8)	− 0.83	− 0.33	− 0.39	1.9×10^9
$[Ir(piq)_2(biq)]^+$ (9)	− 0.79	− 0.29	− 0.35	1.6×10^9

[a] k_q with TEA and TEOA were in the 10^6 M^{-1} s^{-1} range

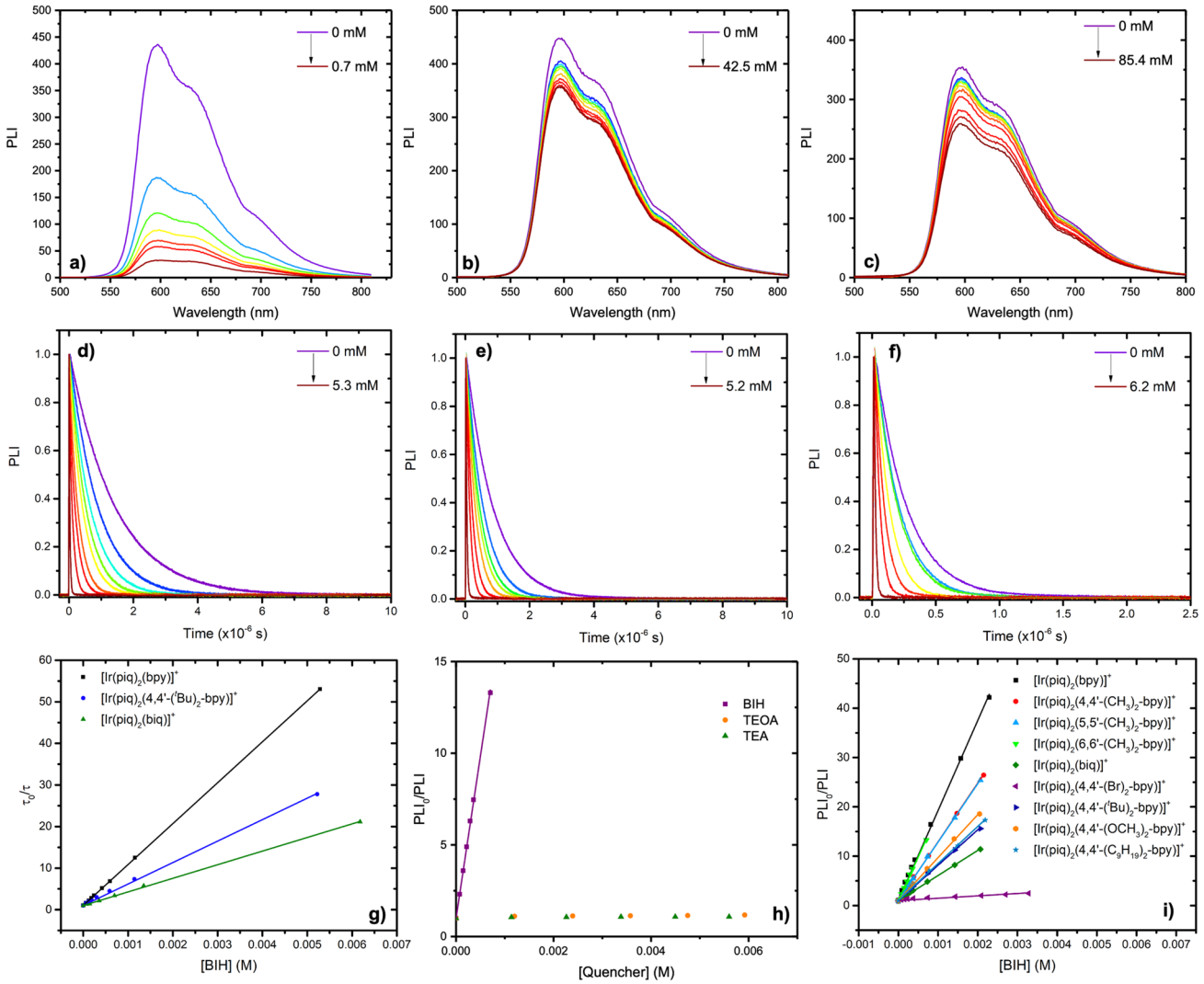


Fig. 4 Excited-state quenching of $[Ir(piq)_2(6,6'\text{-}(CH_3)_2\text{-}bpy)]^+$ with BIH (**a**), TEOA (**b**) and TEA (**c**) in argon purged acetonitrile. The corresponding Stern–Volmer plots is shown in panel (**h**), with the corresponding linear fit for the excited-state quenching in the presence of BIH. The Stern–Volmer plots and corresponding linear fit for the excited-state quenching of all Ir(III) photosensitizers in the presence of BIH is shown in panel (**i**). The time-resolved photoluminescence quenching of $[Ir(piq)_2(bpy)]^+$ (**d**), $[Ir(piq)_2(4,4'\text{-}(^tBu)_2\text{-}bpy)]^+$ (**e**) and $[Ir(piq)_2(biq)]^+$ (**f**), with increasing amounts of BIH, with the corresponding Stern–Volmer plots shown in panel (**g**)

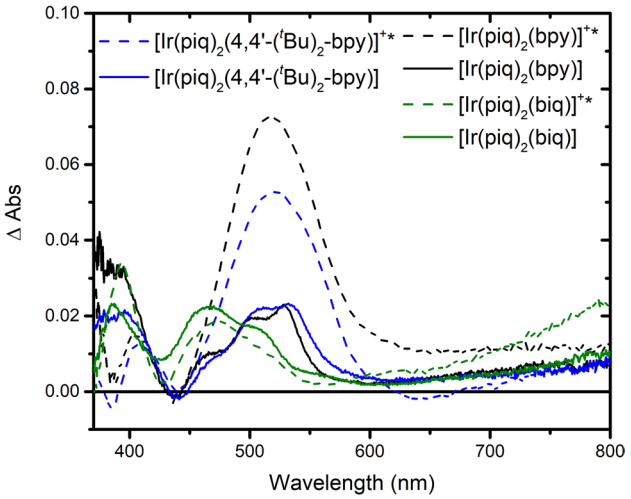


Fig. 5 Transient absorption spectroscopy of $[Ir(piq)_2(bpy)]^+$ (black), $[Ir(piq)_2(4,4'\text{-}(^tBu)_2\text{-}bpy)]^+$ (blue) and $[Ir(piq)_2(biq)]^+$ (olive) recorded 20 ns after the laser pulse in argon purged acetonitrile (dashed) and in the presence of 5.2–6.2 mM BIH (solid)

$[Ir(piq)_2(biq)]^+$ where a smaller k_q was obtained despite having larger ΔG for electron transfer compared to other photosensitizers in the series studied. Although such behavior could be attributed to Marcus inverted region, i.e. decreasing rate constant upon increased exergonicity, this is rarely observed in the case of diffusion controlled bimolecular electron transfer reactions [48–51]. Instead, it was found that the decrease in k_q could likely result from reduced stability of both complexes upon illumination. Indeed, with $[Ir(piq)_2(4,4'\text{-}(Br)_2\text{-}bpy)]^+$ it was observed that allowing more light to excite the photosensitizer, using wider excitation slits, resulted in some degradation that was detected as an increase in photoluminescence upon titration with BIH (see later photostability experiments). To observe genuine quenching, the opening of the excitation slit had to be kept minimal. With $[Ir(piq)_2(biq)]^+$, degradation was not observed with BIH, but with TEA as a quencher, a novel, more energetic photoluminescent band appeared (Fig. S16). Such an observation has already been recorded with $[Ir(ppy)_2(4,4'\text{-}(^tBu)_2\text{-}bpy)]^+$ and $[Ir(ppy)_2(bpy)]^+$ and is more in line with an irreversible reduction of the N^N ligand [52, 53]. To further investigate whether the changes in k_q could originate from degradation processes, we performed time-resolved photoluminescence measurements with $[Ir(piq)_2(biq)]^+$, $[Ir(piq)_2(4,4'\text{-}(^tBu)_2\text{-}bpy)]^+$ and $[Ir(piq)_2(bpy)]^+$ in the presence of increasing amounts of BIH (Fig. 4d-f). The corresponding Stern–Volmer plots were all linear, with quenching rate constants of $7.1\times10^9\ M^{-1}\ s^{-1}$, $6.2\times10^9\ M^{-1}\ s^{-1}$ and $1.3\times10^{10}\ M^{-1}\ s^{-1}$ for $[Ir(piq)_2(bpy)]^+$, $[Ir(piq)_2(4,4'\text{-}(^tBu)_2\text{-}bpy)]^+$ and $[Ir(piq)_2(biq)]^+$, respectively. The values determined via steady-state or time-resolved photoluminescence measurements were the same for $[Ir(piq)_2(bpy)]^+$ and $[Ir(piq)_2(4,4'\text{-}(^tBu)_2\text{-}bpy)]^+$ within experimental errors. However, for $[Ir(piq)_2(biq)]^+$, the quenching rate constant was almost one order of magnitude greater using time-resolved spectroscopy than using steady-state techniques. This change in magnitude could originate from a degradation pathway occurring during steady-state photolysis. Hence, we hypothesized that neither $[Ir(piq)_2(4,4'\text{-}(Br)_2\text{-}bpy)]^+$ nor $[Ir(piq)_2(biq)]^+$ would exhibit reversible behavior upon steady-state illumination and/or photoreduction catalysis, but that the other seven photosensitizers would be attractive candidates.

Nanosecond transient absorption spectroscopy was then used to further confirm that the large quenching rate constants observed with BIH were originating from efficient excited-state electron transfer. Argon-purged solutions of $[Ir(piq)_2(bpy)]^+$, $[Ir(piq)_2(4,4'\text{-}(^tBu)_2\text{-}bpy)]^+$ and $[Ir(piq)_2(biq)]^+$ were exposed to 420 nm pulsed-light excitation to determine their excited-state absorption features (Fig. 5). Both $[Ir(piq)_2(bpy)]^+$ and $[Ir(piq)_2(4,4'\text{-}(^tBu)_2\text{-}bpy)]^+$ exhibited positive absorption features centered around 520 nm. The excited state of $[Ir(piq)_2(biq)]^+$ presented positive absorption features around 460 nm accompanied by large absorption profile at wavelengths greater than 600 nm, consistent with the population of a 2,2′-biquinoline-centered excited-state. In the presence of 5.2–6.2 mM of BIH, pulsed-light excitation led to the formation of the corresponding mono-reduced PS that could easily be observed (Fig. 5). The spectral profile of the mono-reduced PS was in line with other reported spectra of related reduced iridium PS [49, 54–57]. The efficiency of charge separation after electron transfer (cage-escape yield) seems to be in the same range for the three PS, assuming similar molar absorption coefficient for the three mono-reduced PS.

Finally, steady-state illumination was performed to investigate the possibility of reversible accumulation of the mono-reduced photosensitizers. Consequently, solutions of the iridium(III) photosensitizers with an absorbance around 0.5 in the visible region were prepared in argon-purged acetonitrile. BIH was added to reach a concentration of 1 mM. The solutions were then irradiated with commercial blue LED strips for 15 min and absorption spectra were recorded at specific time intervals. Figure 6 shows representative data for $[Ir(piq)_2(bpy)]^+$, $[Ir(piq)_2(4,4'\text{-}(CH_3)_2\text{-}bpy)]^+$, $[Ir(piq)_2(biq)]^+$ and $[Ir(piq)_2(4,4'\text{-}(Br)_2\text{-}bpy)]^+$. Steady-state illuminations with the other photosensitizers are gathered in the supporting information (Figs. S19–S23). With $[Ir(piq)_2(bpy)]^+$ and $[Ir(piq)_2(4,4'\text{-}(CH_3)_2\text{-}bpy)]^+$, blue light excitation led to changes in absorbance that agreed with excited-state electron transfer from BIH to the excited photosensitizers and subsequent mono-reduced complex formation. Indeed, the double absorption peaks at 500 and 530 nm, coupled with the increased absorbance beyond 700 nm were in line with absorption changes

observed in transient absorption spectroscopy with related photosensitizers [49, 54–57]. After 15 min of irradiation, an excess of potassium persulfate ($K_2S_2O_8$) was added as an irreversible electron acceptor to oxidize the monoreduced Ir photosensitizer and recover the ground-state Ir^{III} products. $[Ir(piq)_2(bpy)]^+$ and $[Ir(piq)_2(4,4'\text{-}(CH_3)_2\text{-}bpy)]^+$ showed full reversibility upon the addition of $K_2S_2O_8$, highlighting their great photostability when storing high energy electrons and hence their promise as efficient photosensitizers for applications in reductive catalysis. When $[Ir(piq)_2(4,4'\text{-}(Br)_2\text{-}bpy)]^+$ was used, an increase of the absorbance around 400 nm was rapidly observed with irradiation. Upon addition of $K_2S_2O_8$, this absorption band decreased, but the original spectrum was never recovered, suggesting the instability of this photosensitizer upon prolonged illumination in the presence of electron donors. Finally, $[Ir(piq)_2(biq)]^+$ was also irradiated in the presence of BIH and showed the irreversibility of the photoreduction event (Fig. 6c). As mentioned previously, the irreversibility observed with $[Ir(piq)_2(biq)]^+$ and $[Ir(piq)_2(4,4'\text{-}(Br)_2\text{-}bpy)]^+$ could originate from partial/complete reduction of the N^N diimine ligand under prolonged irradiation, as has already been reported for $[Ir(ppy)_2(4,4'\text{-}(^tBu)_2\text{-}bpy)]^+$ and $[Ir(ppy)_2(bpy)]^+$ using TEA as sacrificial electron donor [52, 53]. The complete reversibility observed for the other photosensitizers speaks towards their robustness and the possibility to use them for solar fuel production such as proton or carbon dioxide reduction.

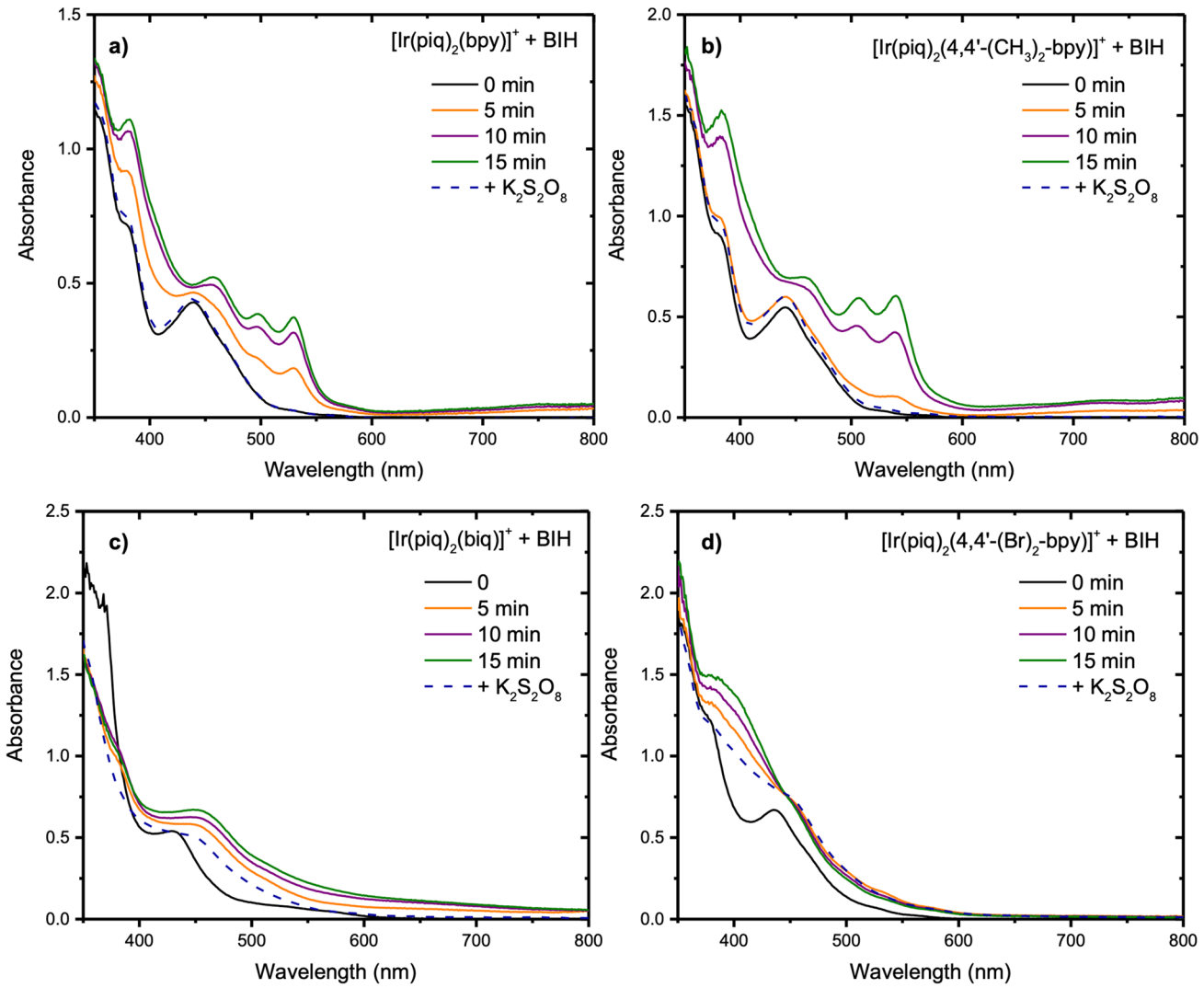


Fig. 6 Absorption spectra of $[Ir(piq)_2(bpy)]^+$ (**a**), $[Ir(piq)_2(4,4'\text{-}(CH_3)_2\text{-}bpy)]^+$ (**b**), $[Ir(piq)_2(biq)]^+$ (**c**) and $[Ir(piq)_2(4,4'\text{-}(Br)_2\text{-}bpy)]^+$ (**d**) in argon-purged acetonitrile at room temperature at $t=0$ min (black) and following 5 min (orange), 10 min (purple) and 15 min (olive) irradiation with blue LED light in the presence of 1 mM BIH. After the irradiation, an excess of $K_2S_2O_8$ was added to oxidize the photo-reduced photosensitizer and investigate reversibility

4 Conclusions

A series of nine $[Ir(piq)_2(LL)]^+$ photosensitizers was synthesized via one common route that involved the synthesis of the $[Ir(piq)_2(\mu\text{-}Cl)]_2$ dimer that further reacted with the N^N ligand. All photosensitizers exhibited appreciable visible light absorption with molar absorption coefficients in the 5400–7900 M^{-1} cm^{-1} range at 427–442 nm. Excited-state quenching with classical electron donors such as TEA, TEOA and BIH was investigated by steady-state excited-state quenching experiments in acetonitrile at ambient temperature. With TEA and TEOA, the quenching rate constants were low ($\sim 10^6$ M^{-1} s^{-1}), but they reached diffusion limited values ($1.9–7.1 \times 10^9$ M^{-1} s^{-1}) when BIH was used. Nanosecond transient absorption spectroscopy in the presence of BIH confirmed that excited-state electron transfer occurred. Steady-state photolysis revealed that compounds with electron withdrawing 2,2′-bipyridine analogues were less stable upon irradiation in the presence of BIH, but the other seven photosensitizers exhibited exceptional dark- and photostability. This stability is vital for photoreduction catalysis, such as solar fuel formation via proton or CO_2 reduction, as reductants with $E_{1/2}(L^{n/n-1})$ between – 1.34 and – 1.47 V vs NHE can be reversibly accumulated. Altogether, the results presented herein show promises for the development of robust photosensitizers for the formation of solar fuels.

Supplementary Information The online version contains supplementary material available at https://doi.org/10.1007/s43630-022-00233-z.

Acknowledgements This work was carried out at the Université catholique de Louvain and the University of North Carolina at Chapel Hill. This work was supported by the Fonds de la Recherche Scientifique (F.R.S.-FNRS) under grant no. U.N021.21 (B.E.) and the Collaborateur Scientifique fellowship (L.T.-G). We acknowledge the use of a nitrogen laser in the CHASE Instrumentation Facility established by the Center for Hybrid Approaches in Solar Energy to Liquid Fuels, CHASE, an Energy Innovation Hub funded by the US Department of Energy, Office of Basic Energy Sciences, Office of Science, under award number DE-SC0021173.

Author contributions The manuscript was written through contributions of all authors. All authors have given approval to the final version of the manuscript.

Declarations

Conflict of interest There are no conflicts to declare.

References

1. Nocera, D. G. (2009). Personalized energy: The home as a solar power station and solar gas station. *Chemsuschem, 2*, 387–390. https://doi.org/10.1002/cssc.200900040
2. Nocera, D. G. (2009). Chemistry of Personalized Solar Energy. *Inorganic Chemistry, 48*, 10001–10017. https://doi.org/10.1021/ic901328v
3. Lewis, N. S., & Nocera, D. G. (2006). Powering the planet: Chemical challenges in solar energy utilization. *Proceedings of the National academy of Sciences of the United States of America, 103*, 15729–15735. https://doi.org/10.1073/pnas.0603395103
4. Armaroli, N., & Balzani, V. (2016). Solar electricity and solar fuels: Status and perspectives in the context of the energy transition. *Chemistry-A European Journal, 22*, 32–57. https://doi.org/10.1002/chem.201503580
5. Ciamician, G. (1912). The photochemistry of the future. *Science, 36*, 385–394. https://doi.org/10.1126/science.36.926.385
6. Meyer, T. J. (1989). Chemical Approaches to Artificial Photosynthesis. *Accounts of Chemical Research, 22*, 163–170. https://doi.org/10.1021/ar00161a001
7. Hammarström, L., & Styring, S. (2011). Proton-coupled electron transfer of tyrosines in photosystem ii and model systems for artificial photosynthesis: The role of a redox-active link between catalyst and photosensitizer. *Energy & Environmental Science, 4*, 2379–2388. https://doi.org/10.1039/C1EE01348C
8. Gust, D., Moore, T. A., & Moore, A. L. (2013). Artificial photosynthesis. *Theoretical and Experimental Plant Physiology, 25*, 182–185.
9. Eberhart, M. S., et al. (2018). Completing a charge transport chain for artificial photosynthesis. *Journal of the American Chemical Society, 140*, 9823–9826. https://doi.org/10.1021/jacs.8b06740
10. Concepcion, J. J., House, R. L., Papanikolas, J. M., & Meyer, T. J. (2012). Chemical approaches to artificial photosynthesis. *Proceedings of the National academy of Sciences of the United States of America, 109*, 15560–15564. https://doi.org/10.1073/pnas.1212254109
11. Wang, D., et al. (2019). Molecular Photoelectrode for water oxidation inspired by photosystem II. *Journal of the American Chemical Society, 141*, 7926–7933. https://doi.org/10.1021/jacs.9b02548
12. Sampaio, R. N., Troian-Gautier, L., & Meyer, G. J. (2018). A Charge-separated state that lives for almost a second at a conductive metal oxide interface. *Angewandte Chemie, 130*, 15616–15620. https://doi.org/10.1002/ange.201807627
13. Shan, B., et al. (2019). Binary molecular-semiconductor p–n junctions for photoelectrocatalytic CO2 reduction. *Nature Energy, 4*, 290–299. https://doi.org/10.1038/s41560-019-0345-y
14. Cancelliere, A. M., et al. (2020). Efficient trinuclear Ru(ii)–Re(i) supramolecular photocatalysts for CO2 reduction based on a new tris-chelating bridging ligand built around a central aromatic ring. *Chemical Science, 11*, 1556–1563. https://doi.org/10.1039/C9SC04532E
15. Sampaio, R. N., Grills, D. C., Polyansky, D. E., Szalda, D. J., & Fujita, E. (2020). Unexpected roles of triethanolamine in the photochemical reduction of CO_2 to formate by ruthenium complexes. *Journal of the American Chemical Society, 142*, 2413–2428. https://doi.org/10.1021/jacs.9b11897
16. Morris, A. J., Meyer, G. J., & Fujita, E. (2009). Molecular approaches to the photocatalytic reduction of carbon dioxide for solar fuels. *Accounts of Chemical Research, 42*, 1983–1994. https://doi.org/10.1021/ar9001679
17. Dempsey, J. L., Brunschwig, B. S., Winkler, J. R., & Gray, H. B. (2009). Hydrogen evolution catalyzed by cobaloximes. *Accounts of Chemical Research, 42*, 1995–2004. https://doi.org/10.1021/ar900253e
18. Teets, T. S., & Nocera, D. G. (2011). Photocatalytic hydrogen production. *Chemical Communications, 47*, 9268–9274. https://doi.org/10.1039/C1CC12390D

19. Heyduk, A. F., & Nocera, D. G. (2001). Hydrogen produced from hydrohalic acid solutions by a two-electron mixed-valence photocatalyst. *Science, 293*, 1639–1641. https://doi.org/10.1126/science.1062965
20. Esswein, A. J., & Nocera, D. G. (2007). Hydrogen production by molecular photocatalysis. *Chemical Reviews, 107*, 4022–4047. https://doi.org/10.1021/cr050193e
21. Fihri, A., et al. (2008). Cobaloxime-based photocatalytic devices for hydrogen production. *Angewandte Chemie International Edition, 47*, 564–567. https://doi.org/10.1002/anie.200702953
22. Fihri, A., Artero, V., Pereira, A., & Fontecave, M. (2008). Efficient H2-producing photocatalytic systems based on cyclometalated iridium- and tricarbonylrhenium-diimine photosensitizers and cobaloxime catalysts. *Dalton Transactions*. https://doi.org/10.1039/B812605B
23. Artero, V., Chavarot-Kerlidou, M., & Fontecave, M. (2011). Splitting water with cobalt. *Angewandte Chemie International Edition, 50*, 7238–7266. https://doi.org/10.1002/anie.201007987
24. Pellegrin, Y., & Odobel, F. (2017). Sacrificial electron donor reagents for solar fuel production. *Comptes Rendus Chimie, 20*, 283–295. https://doi.org/10.1016/j.crci.2015.11.026
25. Razavet, M., Artero, V., & Fontecave, M. (2005). Proton electroreduction catalyzed by cobaloximes: Functional models for hydrogenases. *Inorganic Chemistry, 44*, 4786–4795. https://doi.org/10.1021/ic050167z
26. Sullivan, B. P., Bolinger, C. M., Conrad, D., Vining, W. J., & Meyer, T. J. (1985). One- and two-electron pathways in the electrocatalytic reduction of CO2 by fac-Re(bpy)(CO)3Cl (bpy = 2,2′-bipyridine). *Journal of the Chemical Society, Chemical Communications*. https://doi.org/10.1039/C39850001414
27. Deaton, J. C. & Castellano, F. N. (2017). Archetypal iridium(III) compounds for optoelectronic and photonic applications: photophysical properties and synthetic methods. In: E. Zysman-Colman (Ed.) *Iridium(III) in optoelectronic and photonics applications* (pp. 1–69). Wiley.
28. Bevernaegie, R., Wehlin, S. A. M., Elias, B., & Troian-Gautier, L. (2021). A roadmap towards visible light mediated electron transfer chemistry with iridium(III) Complexes. *ChemPhotoChem, 5*, 217–234. https://doi.org/10.1002/cptc.202000255
29. Prier, C. K., Rankic, D. A., & MacMillan, D. W. C. (2013). Visible light photoredox catalysis with transition metal complexes: Applications in organic synthesis. *Chemical Reviews, 113*, 5322–5363. https://doi.org/10.1021/cr300503r
30. Lentz, C., Schott, O., Auvray, T., Hanan, G., & Elias, B. (2017). Photocatalytic hydrogen production using a red-absorbing Ir(III)–Co(III) Dyad. *Inorganic Chemistry, 56*, 10875–10881. https://doi.org/10.1021/acs.inorgchem.7b00684
31. Sauvageot, E., et al. (2016). Iridium complexes inhibit tumor necrosis factor-α by utilizing light and mixed ligands. *Journal of Organometallic Chemistry, 808*, 122–127. https://doi.org/10.1016/j.jorganchem.2016.02.001
32. Lin, S., et al. (2015). Luminescence switch-on detection of protein tyrosine kinase-7 using a G-quadruplex-selective probe. *Chemical Science, 6*, 4284–4290. https://doi.org/10.1039/C5SC01320H
33. Lu, L., et al. (2014). Detection of nicking endonuclease activity using a G-quadruplex-selective luminescent switch-on probe. *Chemical Science, 5*, 4561–4568. https://doi.org/10.1039/C4SC02032D
34. Lin, S., et al. (2015). Luminescence switch-on assay of interferon-gamma using a G-quadruplex-selective iridium(iii) complex. *Chemical Communications, 51*, 16033–16036. https://doi.org/10.1039/C5CC06655G
35. Liu, L.-J., et al. (2015). An Iridium(III) Complex inhibits JMJD2 activities and acts as a potential epigenetic modulator. *Journal of Medicinal Chemistry, 58*, 6697–6703. https://doi.org/10.1021/acs.jmedchem.5b00375
36. Zhao, Q., et al. (2006). Series of New Cationic Iridium(III) complexes with tunable emission wavelength and excited state properties: Structures, theoretical calculations, and photophysical and electrochemical properties. *Inorganic Chemistry, 45*, 6152–6160. https://doi.org/10.1021/ic052034j
37. Nonoyama, M. (1974). Benzo[h]quinolin-10-yl-N Iridium(III) complexes. *Bulletin of the Chemical Society of Japan, 47*, 767–768. https://doi.org/10.1246/bcsj.47.767
38. Bevernaegie, R., et al. (2018). Ultrafast charge transfer excited state dynamics in trifluoromethyl-substituted iridium(iii) complexes. *Physical Chemistry Chemical Physics: PCCP, 20*, 27256–27260. https://doi.org/10.1039/C8CP04265A
39. Bevernaegie, R., et al. (2018). Trifluoromethyl-substituted iridium(III) complexes: From photophysics to photooxidation of a biological target. *Inorganic Chemistry, 57*, 1356–1367. https://doi.org/10.1021/acs.inorgchem.7b02778
40. Brouwer, A. M. (2011). Standards for photoluminescence quantum yield measurements in solution (IUPAC Technical Report). *Pure and Applied Chemistry, 83*, 2213–2228. https://doi.org/10.1351/PAC-REP-10-09-31
41. Franco, C., & Olmsted, J. (1990). Photochemical determination of the solubility of oxygen in various media. *Talanta, 37*, 905–909. https://doi.org/10.1016/0039-9140(90)80251-A
42. Juris, A., et al. (1988). Ru(II) polypyridine complexes: Photophysics, photochemistry, eletrochemistry, and chemiluminescence. *Coordination Chemistry Reviews, 84*, 85–277. https://doi.org/10.1016/0010-8545(88)80032-8
43. Campagna, S., Puntoriero, F., Nastasi, F., Bergamini, G. & Balzani, V. (2007). Photochemistry and photophysics of coordination compounds: Ruthenium. In: V. Balzani & S. Campagna (Eds.), *Photochemistry and photophysics of coordination compounds I* (pp. 117–214). Springer Berlin Heidelberg.
44. Yarnell, J. E., McCusker, C. E., Leeds, A. J., Breaux, J. M., & Castellano, F. N. (2016). Exposing the excited-state equilibrium in an IrIII bichromophore: A combined time resolved spectroscopy and computational study. *European Journal of Inorganic Chemistry*. https://doi.org/10.1002/ejic.201600194
45. McCusker, C. E., Chakraborty, A., & Castellano, F. N. (2014). Excited state equilibrium induced lifetime extension in a dinuclear platinum(II) complex. *Journal of Physical Chemistry A, 118*, 10391–10399. https://doi.org/10.1021/jp503827e
46. Kuramochi, Y., & Ishitani, O. (2016). Iridium(III) 1-Phenylisoquinoline complexes as a photosensitizer for photocatalytic CO_2 reduction: A mixed system with a Re(I) catalyst and a supramolecular photocatalyst. *Inorganic Chemistry, 55*, 5702–5709. https://doi.org/10.1021/acs.inorgchem.6b00777
47. Giereth, R., et al. (2021). Exploring the full potential of photocatalytic carbon dioxide reduction using a dinuclear Re2Cl2 complex assisted by various photosensitizers. *ChemPhotoChem, 5*, 644–653. https://doi.org/10.1002/cptc.202100034
48. Takeda, N., & Miller, J. R. (2020). Inverted region in bimolecular electron transfer in solution enabled by delocalization. *Journal of the American Chemical Society, 142*, 17997–18004. https://doi.org/10.1021/jacs.0c04780
49. Bevernaegie, R., et al. (2020). Improved visible light absorption of potent iridium(III) photo-oxidants for excited-state electron transfer chemistry. *Journal of the American Chemical Society, 142*, 2732–2737. https://doi.org/10.1021/jacs.9b12108
50. Piechota, E. J., & Meyer, G. J. (2019). Introduction to electron transfer: Theoretical foundations and pedagogical examples. *Journal of Chemical Education, 96*, 2450–2466. https://doi.org/10.1021/acs.jchemed.9b00489
51. Closs, G. L., & Miller, J. R. (1988). Intramolecular long-distance electron transfer in organic molecules. *Science, 240*, 440–447. https://doi.org/10.1126/science.240.4851.440

52. Aydogan, A., et al. (2021). Mechanistic investigation of a visible light mediated dehalogenation/cyclisation reaction using iron(iii), iridium(iii) and ruthenium(ii) photosensitizers. *Catalysis Science & Technology, 11*, 8037–8051. https://doi.org/10.1039/D1CY01771C
53. Connell, T. U., et al. (2019). The tandem photoredox catalysis mechanism of [Ir(ppy)2(dtb-bpy)]+ enabling access to energy demanding organic substrates. *Journal of the American Chemical Society, 141*, 17646–17658. https://doi.org/10.1021/jacs.9b07370
54. Xu, B., et al. (2020). Photocatalyzed diastereoselective isomerization of cinnamyl chlorides to cyclopropanes. *Journal of the American Chemical Society, 142*, 6206–6215. https://doi.org/10.1021/jacs.0c00147
55. Morton, C. M., et al. (2019). C-H alkylation via multisite-proton-coupled electron transfer of an aliphatic C–H Bond. *Journal of the American Chemical Society, 141*, 13253–13260. https://doi.org/10.1021/jacs.9b06834
56. Deetz, A. M., Troian-Gautier, L., Wehlin, S. A. M., Piechota, E. J., & Meyer, G. J. (2021). On the determination of halogen atom reduction potentials with photoredox catalysts. *Journal of Physical Chemistry A, 125*, 9355–9367. https://doi.org/10.1021/acs.jpca.1c06772
57. Hankache, J., Niemi, M., Lemmetyinen, H., & Wenger, O. S. (2012). Photoinduced electron transfer in linear triarylamine–photosensitizer–anthraquinone triads with ruthenium(II), osmium(II), and iridium(III). *Inorganic Chemistry, 51*, 6333–6344. https://doi.org/10.1021/ic300558s